ENGINEERING

Reconfigurable modular origami for tunable 2D symmetry groups

Weiqi Liu[1,2]†, Qun Ren[3]†, Yunjie Wang[4], Zhuang Zhang[4], Xiuyu Wang[5], Yongshan Liang[3], Hao Huang[5], Jiayao Ma[1,2], Hanqing Jiang[4]*, Yan Chen[1,2]*

Symmetry correlates with the physical properties in many fields, such as electromagnetics, optics, acoustics, etc.; thus, tunability among different symmetry groups is highly desired in the corresponding systems to achieve multiple functionalities. However, among the limited cases of altering symmetry motifs, the major methods rely on the refabrication or reassembly. Here, inspired by modular origami, we propose a set of single-degree of freedom (DOF) reconfigurable modules with rich symmetry configurations through the inherent kinematic bifurcation. Subsequently, all 17 space groups in the Euclidean plane can be achieved with only two sets of module tessellations, which can be reversibly tuned by a simple binary pressurization strategy for air pouches. Furthermore, the selection rules of multipole quasibound states in the continuum via symmetry group tuning in metasurface are established by combining electromagnetic antennas. This work opens a promising avenue to program the properties of reconfigurable metastructures based on tunable symmetry.

INTRODUCTION

Symmetry is a ubiquitous phenomenon, deeply rooted in natural plants, animals, artificial architecture, Islamic motifs, and so on (*1*, *2*). In mathematics, symmetry typically refers to geometric objects that are invariant under certain operations or transformations, such as translation, rotation, or glide reflection. On the Euclidean plane, there are only three classes of discrete symmetry groups in periodic structures, which encompass all transformations under which an object remains invariant (*3*, *4*). These three symmetry groups include two families of rosette groups [two-dimensional (2D) point groups], 7 frieze groups (2D line groups), and 17 wallpaper groups (2D space groups) in finite designs, monotranslational designs, and bitranslational designs, respectively. The presence of symmetry in geometric shapes not only contributes to their aesthetic appeal but also serves as a fundamental concept underpinning numerous scientific principles and applications across various scales and disciplines (*5*, *6*), ranging from predicting the properties of crystals (*7*), enhancing the physical properties of engineering structures (*8*, *9*), designing architected materials with extreme properties (*10*, *11*), manipulating the electromagnetic (EM) properties of metamaterials (*12*–*16*), to inducing higher-order topological phases (*17*–*19*).

Because symmetry is closely coupled with the system's specific properties, the tunability among different symmetry groups can certainly induce multiple functionalities, such as stable signal propagation, diverse nonreciprocal effects in reversible mechanical diode (*20*), and anisotropic morphing in metamaterials (*21*), while also underpinning the study of symmetry-protected bound states in the continuum (BICs) and their transformation into quasi-BICs (qBICs) (*22*–*24*), which has attracted notable interest recently. However, it is still a major challenge to achieve dynamic symmetry tunability. At the macroscale, unit cells of rotating square structures can transform between nonchiral and opposite chiral morphologies under tensile strain, enabling deformable metamaterials with advanced applications in dynamic near-field imaging and tunable double-focus metalenses (*25*). There is no system able to transform among all symmetry groups with generality, scalability, reversibility, and low energy consumption. For the micro- and nanoscale systems, one example is that by changing the environmental temperature, microgeometric parameters of the Kagome structure can be varied, leading to symmetry tuning and programmable Poisson's ratio of the structure (*26*, *27*). At the current stage, the low actuating force restricts the capacity of deformation between limited symmetry configurations.

Kinematic-based origami, with its flexible design space, powerful deformation capability, and wide range of property tunability, also plays a crucial role in designing architected structures with tunable symmetry (*28*–*31*). Previous efforts have exploited shape transformation of rigid origami to tune chirality (*32*, *33*). Nevertheless, the ability of such structures to tune symmetry groups is somewhat limited, as they can only be deformed between two final configurations. Reconfigurable origami, with its ability to undergo multiple shape transformations through crease topological morphing or introduced strategic cuts (*34*–*37*), holds great promise for achieving tunability over a broader range of symmetry groups within a single structure (*38*, *39*). However, constrained by the geometry of the original pattern or the control complexity of the multi-DOF system, these typically rely on manual manipulation and are limited to several symmetry configurations. Therefore, dynamically and reversibly accessing a broad spectrum of symmetry groups, especially across all 17 wallpaper groups, remains an open question.

To address these challenges, we turn to modular origami, a subfield of origami that involves folding multiple sheets into individual units or blocks that are subsequently assembled into a transformable structure (*40*–*45*). Unlike traditional origami, where the basic unit of kinematic analysis is a vertex, modular origami shifts the fundamental analysis unit to independent closed-loop systems formed by rigid components around cuts or holes. These closed loops are

[1]School of Mechanical Engineering, Tianjin University, Tianjin 300350, China. [2]Key Lab for Mechanism Theory and Equipment Design of Ministry of Education, Tianjin University, Tianjin 300350, China. [3]School of Electrical and Information Engineering, Tianjin University, Tianjin 300072, China. [4]School of Engineering, Westlake University, Hangzhou, Zhejiang 310030, China. [5]Tianjin Key Laboratory of Imaging and Sensing Microelectronic Technology, School of Microelectronics, Tianjin University, Tianjin 300072, China.
*Corresponding author. Email: hanqing.jiang@westlake.edu.cn (H.J.); yan_chen@tju.edu.cn (Y.C.)
†These authors contributed equally to this work.

kinematically equivalent to planar, spherical, or spatial linkages, providing enhanced reconfiguration capabilities. In particular, the single-DOF module origami with kinematic bifurcation not only enables rich symmetry configuration changes but also offers a simple yet efficient actuation strategy for reconfigurable structures. In this work, we developed a set of single-DOF reconfigurable modular origami by connecting blocks into a spatial 7–revolute (*7R*) linkage, capable of realizing rich symmetry configurations through kinematic bifurcation. By tessellating only two sets of these modules, we demonstrate the dynamic generation of all 17 wallpaper groups in the Euclidean plane via a simple and efficient actuation strategy. Furthermore, we establish selection rules for multipole qBICs via symmetry tuning in metasurfaces, leveraging the interplay between symmetry and EM antenna design. Our approach provides a promising paradigm for tunable symmetry in reconfigurable metastructures, paving the way for programmable physical properties across diverse applications.

RESULTS

Design of the modular origami unit and the *n*-unit symmetry modules

The design of a modular origami unit is fundamentally guided by the concept of kinematic bifurcation (*46*), where a mechanism can evolve into multiple motion paths due to its inherent geometric constraints. Linkages with kinematic bifurcations are usually accompanied by symmetric geometric parameters, and such bifurcation-induced reconfiguration often causes symmetry breaking in the configuration. To harness this characteristic, we constructed a plane-symmetric spatial *7R* linkage specifically configured to support bifurcation (Fig. 1A). Then, the geometric parameters (a, b, and α) of the target spatial *7R* linkage are mapped onto modular origami components, which are then sequentially assembled to realize the desired kinematic behavior, including bifurcations. Specifically, as shown in Fig. 1A, we construct a modular origami unit by bonding two thin rectangular sheets (side length $a \times t_2$), two rectangular blocks (side length $t_1 \times t_2 \times t_3$), and two triangular panels (base length b, base angles β and γ, thickness t_1) around an isosceles trapezoidal panel [angle α between the two legs, leg length t_2, thickness t_4, shorter base length $2a\cos(\alpha/2)$] sequentially to form a closed loop. Assuming that all components are rigid and can fold only along the connected edges, which act as revolute joints with axes indicated by red center lines, this modular origami unit is kinematically equivalent to a spatial *7R* linkage with one DOF (fig. S1). Hence, dihedral φ_1 ($\varphi_1 \in [0, \pi]$) can be taken as the input to determine its motion with the kinematic curves shown in Fig. 1B. However, when the two rectangular sheets are vertical at configuration B_0 with $\varphi_1 = \varphi_2 = \varphi_3 = \varphi_4 = \pi/2$, a

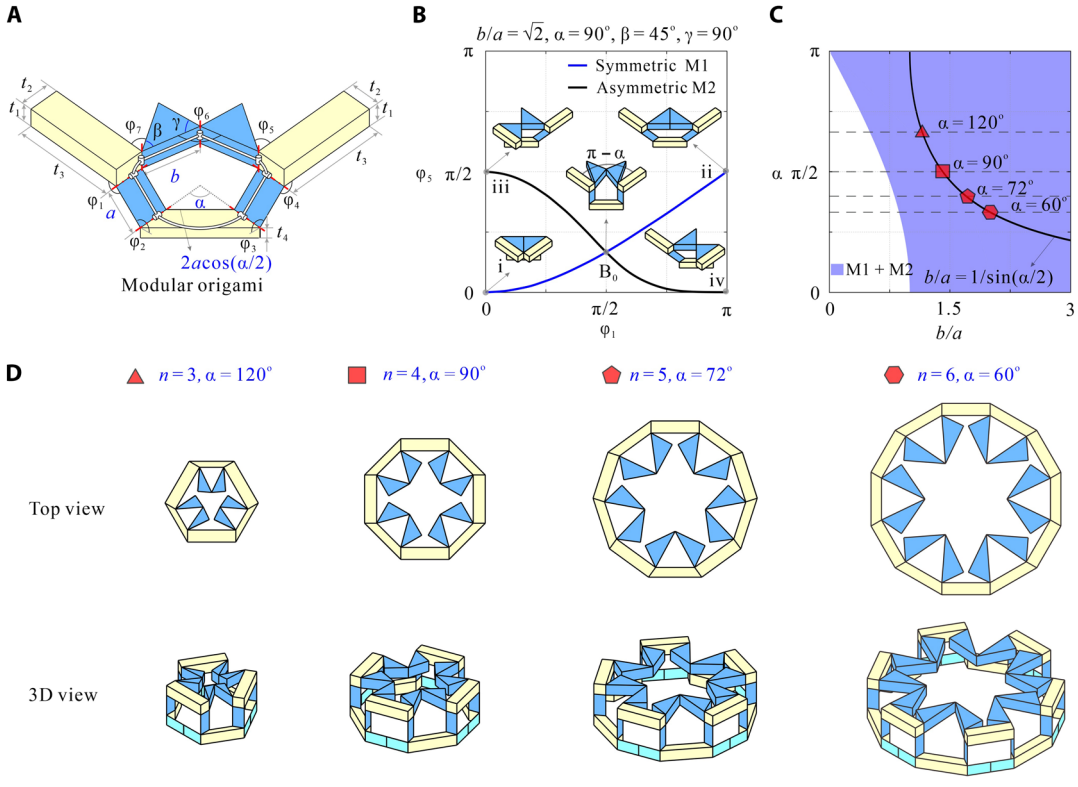

Fig. 1. Construction of *n*-unit ($n = 3, 4, 5,$ and 6) symmetry modules using a modular origami unit with kinematic bifurcation. (**A**) Components of a modular origami unit and its geometry. A single modular origami unit is composed of two thin rectangular sheets (side length $a \times t_2$), two rectangular blocks (side length $t_1 \times t_2 \times t_3$), two triangular panels (base length b, base angles β and γ, thickness t_1), and an isosceles trapezoidal panel [angle α between the two legs, leg length t_2, thickness t_4, shorter base length $2a\cos(\alpha/2)$]. Axes of joints are indicated by red center lines. (**B**) Motion path φ_5 versus φ_1 and corresponding configurations of the modular origami unit with $b/a = \sqrt{2}$, $\alpha = 90°$, $\beta = 45°$, and $\gamma = 90°$. Configurations i, ii, iii, and iv are motion sequences, while configuration B_0 is the bifurcation point. (**C**) Design space where a modular origami unit can be reconfigured between M1 and M2 paths. The blue area represents $b/a > \cos(\alpha/2)$, and the markers represent $b/a = 1/\sin(\alpha/2)$ when $\alpha = 120°$, 90°, 72°, and 60°. (**D**) Construction of *n*-unit ($n = 3, 4, 5,$ and 6) symmetry modules with an unfolded $2n$-sided shape. The additional thin rectangular sheets (side length $a \times t_4$) used to connect the two neighboring modular origami units are shown in ice blue.

kinematic bifurcation occurs, as revealed by closure equations of the 7*R* linkage (text S1). If two rectangular sheets swing in the opposite directions, then the unit follows a plane-symmetric path M1, the blue path i-B_0-ii, governed by the dihedral angle relationship that

$$\begin{aligned}&\varphi_1=\varphi_2=\varphi_3=\varphi_4,\varphi_5=\varphi_7\\&\varphi_5=\varphi_7=\left(\pi+\varphi_6-a\right)/2-\beta\\&\varphi_6=2\arcsin\frac{\left(a\cos\varphi_1+a\right)\cos(a/2)}{b}\end{aligned}\tag{1}$$

Conversely, if the sheets swing in the same direction, then the unit involves the asymmetric path M2, the black path iii-B_0-iv, governed by the dihedral angle relationship that

$$\begin{aligned}&\varphi_1=\varphi_2=\pi-\varphi_3=\pi-\varphi_4\\&\varphi_6=2\arcsin\sqrt{\frac{a^2\left(\cos^2\varphi_1+1\right)-a^2\cos a\left(\cos^2\varphi_1-1\right)}{2b^2}}\\&\varphi_5=\frac{\pi}{2}+\frac{\varphi_6}{2}-\arccos\frac{2a^2\cos\varphi_1-b^2+b^2\cos\varphi_6}{2ab\sin\frac{\varphi_6}{2}\left(\cos_{\varphi_1}-1\right)}-\beta\\&\varphi_7=\frac{\pi}{2}+\frac{\varphi_6}{2}-\arccos\frac{2a^2\cos\varphi_1+b^2-b^2\cos\varphi_6}{2ab\sin\frac{\varphi_6}{2}\left(\cos\varphi_1+1\right)}-\beta\end{aligned}\tag{2}$$

The bifurcation between the symmetric path M1 and the asymmetric path M2 exists when $b/a > \cos(\alpha/2)$, corresponding to the blue region in Fig. 1D (for detailed analysis, see figs. S2 to S4 and text S2). For general design parameters, the modular origami unit exhibits richer bifurcations, involving paths M1 to M5, as illustrated by the representative configurations and motion sequences in fig. S5 and text S3. Paths M1/M2 and M3/M4 are differentiated by whether the triangular panels adopt bulged-out or nested-in configurations, respectively; however, these result in equivalent symmetry configurations, rendering them redundant from a functional standpoint. Besides, path M5 is kinematically invalid due to panel interference. Considering that the triangular panels in the M3 and M4 paths obstruct the assembly of wallpaper groups, we set geometric parameters to $b/a > \cos(\alpha/2)$, $\beta = (\pi - \alpha)/2$, and $\gamma \geq \alpha/2$, thereby retaining only the M1 and M2 paths.

The kinematic analysis reveals that two rectangular blocks are always horizontally positioned and maintain an angle $\pi - \alpha$ whether moving along the M1 or M2 path (fig. S6). Therefore, we can construct *n*-unit symmetry modules by arranging *n* modular origami units with $\alpha = 2\pi/n$ in a circular array, where each pair of neighboring units shares a common rectangular block. Here, only $n = 3$, 4, 5, and 6 are considered to cover the whole 2D symmetry groups. Subsequently, these symmetry modules form a 2*n*-sided profile in the top views of Fig. 1D. To achieve a compact folded configuration, $b/a = 1/\sin(\alpha/2)$ (black line in Fig. 1C), $\beta = (\pi - \alpha)/2$, $\gamma = \alpha/2$, and $t_3 = 2a$ must be met. Without loss of generality, we can set that all modular origami units have $t_1 = t_2 = t_4 = a/2$. To ensure that the mechanical assembly of *n* units retains a single DOF, we inserted two additional ice-blue sheets, each with length *a*, between neighboring units to form a 7*R* closed loop with $\alpha = 0$. The motion sequence of the 7*R* unit is depicted in fig. S7. The configurations of the 7*R* unit with $\alpha = 0$ are not independent; instead, they are defined by the swing direction of the blue rectangular sheets in the two neighboring modular origami units with $\alpha = 2\pi/n$. Eventually, a set of single-DOF *n*-unit ($n = 3$, 4, 5, and 6) symmetry modules is constructed, as shown in the 3D views in Fig. 1D.

Reconfiguration of *n*-unit symmetry modules with tunable 2D point groups

Because of the *n*-fold symmetry in the *n*-unit module composed of identical units, both the kinematic compatibility and bifurcation are well preserved. For the four-unit symmetry module in Fig. 2A, the top configuration is the bifurcation point, as four modular origami units with $\alpha = 90°$ are all in the bifurcation configuration, i.e., each of them can choose to move either in the M1 or M2 path. This results in $2^4 = 16$ combinations. For a 7*R* unit with $\alpha = 0$ used for connection, its motion depends on whether two neighboring modular origami units move within the range $\varphi_1 \in [0, \pi/2)$ or $\varphi_1 \in (\pi/2, \pi]$. This expands the total combinations to $2 \times 16 = 32$. However, two conditions for kinematic compatibility must be satisfied at the same time: (i) The motion transmitted through the transmission loop finally returns to the input, and (ii) *n* modular origami units need to form a closed-loop polygon throughout the folding and unfolding process (fig. S8 and text S4). Because of the limitation in the side lengths of the ice-blue rectangular sheets, simultaneous inward folding of the blue sheets on both sides of any 7*R* unit with $\alpha = 0$ violates the second condition (fig. S9). Therefore, only 25 combinations are compatible. Among the 25 compatible combinations, 18 cases can overlap with themselves through rotation or reflection symmetry operations (fig. S10). Last, only the seven configurations at the bottom of Fig. 2A are distinct.

Figure 2A shows the reconfiguration process among seven distinct configurations through a common bifurcation point of the four-unit symmetry module (movie S1), while Fig. 2B plots the corresponding geometric dimensional variations, i.e., the width (*W*), breadth (*B*), and height (*H*) in the *x*, *y*, and *z* directions (text S5). It can be observed that when all four modular origami units U_1 to U_4 move along the plane-symmetric path M1 governed by φ_1 where $\varphi_1 \in [0, \pi/2]$, the four-unit symmetry module exhibits *d*4 point group (*dn* indicates both *n*-fold rotational and reflectional symmetry), as shown in Fig. 2A. In this case, the compatible module expands bidirectionally from a smaller square in the *xoy* plane to a larger one until it reaches bifurcation configuration, also the configuration with maximum height, as shown by the blue curve representing B_I and W_I in Fig. 2B. If two alternating units, e.g., units U_2 and U_4 in case II, switch to the asymmetric M2 path after passing through the bifurcation point, while the other two units remain in the symmetric path M1 where $\varphi_1 \in [0, \pi/2)$, then the four-unit symmetry module still satisfies the kinematic compatibility conditions, but its symmetry reduces to *c*2 point group (*cn* indicates only *n*-fold rotational symmetry). Conversely, if it is neighboring units rather than alternating units, such as U_1 and U_4 in case III, which switch to the asymmetric path M2, then the symmetry of the compatible four-unit symmetry module becomes *d*1 point group. In these two cases, only one of two dimensions in the *xoy* plane changes, e.g., B_II and B_III in cases II and III (blue curve in Fig. 2B), while W_II and W_III are invariant to changes in height (black curve in Fig. 2B). Other compatible possibilities are cases IV to VII, as listed in Fig. 2A. Specifically, when the configuration of all four units is in the asymmetric path M2, the symmetry is denoted as *c*4 [case IV in Fig. 2 (A and B)]. In case V, although all four modular origami units U_1 to U_4 move along the plane-symmetric path M1, unlike in case I, the two alternating units (e.g., U_2 and U_4) belong to $\varphi_1 \in [0, \pi/2)$, and the other two units belong to $\varphi_1 \in (\pi/2, \pi]$. In this case, the module exhibits *d*2 point group. Furthermore, the compatible cases VI and VII are similar to cases II and III, respectively, with the difference that

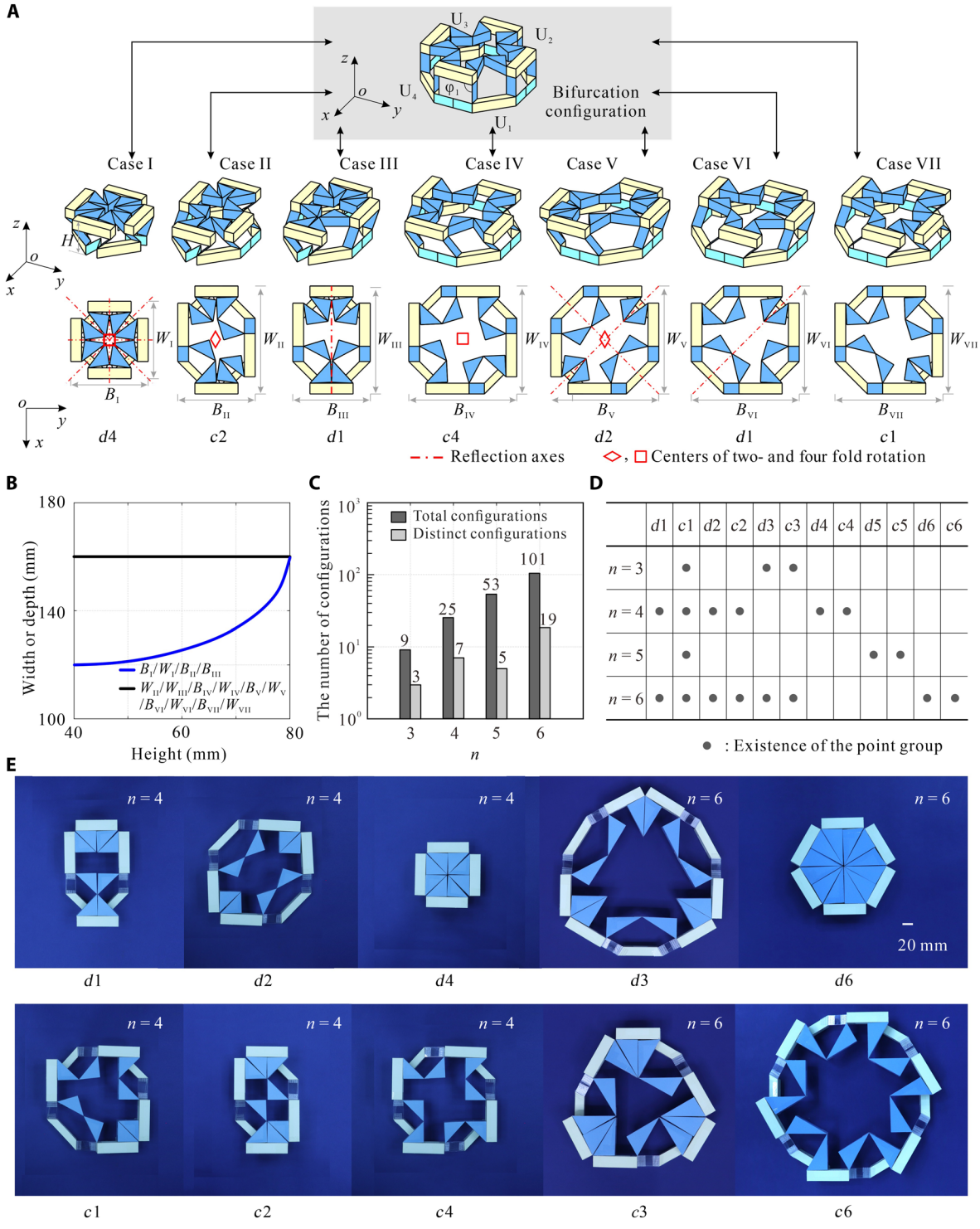

Fig. 2. Reconfigurable *n*-unit symmetry module with tunable 2D point symmetry groups. (**A**) Reconfiguration of the four-unit symmetry module accompanied by tunable symmetry. Seven distinct configurations originate from the same bifurcation point, i.e., the top configuration, where all four units simultaneously sit at $\varphi_1 = 90°$. The key reflection axes are represented by center lines, while the centers of two- and fourfold rotational symmetry are represented by rhombuses and squares, respectively. (**B**) The variation of the geometric dimensions, i.e., the width (*W*) and breadth (*B*) in *x* and *y* directions, with the height (*H*). (**C**) The total number of configurations and distinct configurations versus the number *n* of units within the module. (**D**) Point group distribution of bifurcation configurations of *n*-unit symmetry modules, where gray dots represent the existence of point groups. (**E**) Prototypes with 10 2D crystallographic point groups, i.e., *d*1, *d*2, *d*3, *d*4, *d*6, *c*1, *c*2, *c*3, *c*4, and *c*6, constructed from four- and six-unit symmetry modules.

one of the two units in the M1 path belongs to $\varphi_1 \in [0, \pi/2)$, and the other belongs to $\varphi_1 \in (\pi/2, \pi]$. Consequently, their symmetries are $d1$ and $c1$ point groups, respectively. In cases IV to VII, both dimensions $B_{IV}/B_V/B_{VI}/B_{VII}$ and $W_{IV}/W_V/W_{VI}/W_{VII}$ in the *xoy* plane are invariant to changes in height, as shown by the black curve in Fig. 2B. In summary, there are a total of 25 cases that satisfy kinematic compatibility conditions (fig. S10) for the four-unit symmetry module, but due to the similarity of the orthogonal directions, there are only seven different bifurcation configurations and six types of point groups, i.e., $d4$, $c4$, $d2$, $c2$, $d1$, and $c1$ point groups.

We also investigated kinematic bifurcation and symmetry changes for three-, five-, and six-unit symmetry modules (fig. S11). Figure 2C summarizes their total number of configurations and distinct configurations, while Fig. 2D shows the point group distribution of these configurations of n-unit symmetry modules. As n increases from 3 to 6, the number of total configurations also grows rapidly from 9 to 101. Specifically, the three-unit symmetry module exhibits $d3$, $c3$, and $c1$ point groups, the five-unit symmetry module exhibits $d5$, $c5$, and $c1$ point groups, while the six-unit symmetry module exhibits $d6$, $c6$, $d3$, $c3$, $d2$, $c2$, $d1$, and $c1$ point groups (gray dots in Fig. 2D). Because of these symmetry properties, the number of distinct configurations for n-unit symmetry modules reduces markedly. In general, arranging n modular origami units with $\alpha = 2\pi/n$ into a circular array around the z axis obtains the n-unit symmetry module with arbitrary dn or cn point groups (two families of rosette groups). Owing to the powerful kinematic bifurcation, four- and six-unit symmetry modules are sufficient to cover all 10 2D crystallographic point groups, i.e., $d1$, $d2$, $d3$, $d4$, $d6$, $c1$, $c2$, $c3$, $c4$, and $c6$, which are demonstrated by prototypes in Fig. 2E (for fabrication details, see Materials and Methods).

Module tessellations with tunable 2D line and space groups

Building upon the symmetry modules, an important challenge is to determine whether these reconfigurable modules can be systematically tessellated to achieve all 7 frieze patterns or 17 wallpaper patterns in a unified platform (*3*, *4*). We address this challenge by leveraging consistent geometric connection rules, i.e., merging rectangular blocks while tuning the local bifurcation states of the modules to modulate global symmetry. This strategy enables the creation of a reconfigurable metastructure in which multiple symmetry groups can be accessed from a single physical implementation.

In mathematics, there are exactly seven frieze groups (also known as 2D line groups), denoted as $p111$, $p1a1$, $pm11$, $p1m1$, $p112$, $pma2$, and $pmm2$. A systematic classification of these groups is provided in table S1. Using only the four-unit symmetry module in a linear tessellation, we successfully reproduce all seven frieze groups (gray strip in Fig. 3A and construction details in fig. S12). The frieze pattern with the $p111$ line group is formed by repeatedly applying a translation to the four-unit symmetry module with $c1$ point group under the condition of merging rectangular blocks. If the geometric operation to the modules with $c1$ point group is glide reflection and translation, then the symmetry of the resulting frieze pattern becomes $p1a1$ line group. Similarly, applying continuous reflections of the module with $c1$ point group about vertical reflection axes results in $pm11$ line group. If the module with $c1$ point group is reconstructed to the state with $c2$ or $d1$ point group and is in a translational arrangement, the resulting frieze pattern exhibits $p112$ or $p1m1$ line groups. In contrast, if it is not a translational arrangement but a continuous reflection, then the frieze pattern exhibits $pma2$ or $pmm2$ line groups. Despite their symmetry differences, all seven frieze groups are derived from a four-unit symmetry module with identical connections. Thus, the seven frieze groups can be interconverted through local bifurcation-induced reconfiguration.

Now, let us consider a geometric object that repeats regularly through translation in two nonparallel directions. It has been demonstrated that any infinite 2D pattern belongs to one of the 17 distinct wallpaper groups, also known as planar crystallographic groups, or 2D space groups, classified by combinations of translation, rotation, reflection, and glide reflection (table S2). On one hand, a subset of these wallpaper groups, specifically those with one- or twofold rotational symmetry, can be systematically constructed by extending the seven frieze patterns described earlier. For instance, under the condition of merging rectangular blocks, the $p1$, pg, and pm wallpaper groups are obtained by vertically stacking the frieze patterns $p111$, $p1a1$, and $pm11$, respectively, in an orderly fashion (Fig. 3A). The $p2$ group arises by vertically shifting copies of the frieze pattern $p112$. Meanwhile, reflection-based operations applied to $p1a1$, $pmm2$, and $pma2$ generate the cm, pmm, and cmm wallpaper groups, respectively. Glide reflections of $p1m1$ and $p1a1$ produce the pmg and pgg wallpaper groups. On the other hand, fourfold wallpaper patterns can be realized by combining motifs with lower symmetry using combinatorial operations or by directly using motifs with higher symmetry. For example, the $p4g$ wallpaper group can be constructed by rotating a four-unit symmetry module with $c2$ point group four times, followed by bidirectional translations. Alternatively, directly repeating modules with $c4$ or $d4$ point groups in both directions yields the $p4$ or $p4m$ wallpaper groups. Using this framework, we constructed 12 of the 17 wallpaper groups with one-, two-, and fourfold rotational symmetry based on four-unit symmetry modules (Fig. 3A). In these constructions, the modules are connected in the same way across different wallpaper groups, meaning that these 12 2D space groups can all be realized through a single structure (movie S2). Besides, all modules in specific wallpaper groups have the same dimensional variation in the x or y direction according to Fig. 2B, so the tessellations are compatible. However, the remaining five wallpaper groups ($p3$, $p3m1$, $p31m$, $p6$, and $p6m$), which require three- or sixfold rotational symmetry, cannot be generated using four-unit modules. To achieve these symmetries, we introduce either a three-unit symmetry module (fig. S13) or a six-unit symmetry module. Figure 3B illustrates examples of constructing these five additional wallpaper groups using six-unit symmetry modules. The beehive structure is formed with six identical modules in a circle around the center module by merging rectangular blocks. Depending on whether the center module has $c3$, $d3$, $c6$, or $d6$ point groups, the obtained beehive structure belongs to the $p3$, $p3m1$, $p6$, or $p6m$ wallpaper groups. The $p31m$ wallpaper group is constructed a little differently in that the center module has $d6$ symmetry and surrounding it are six modules with $c3$ symmetry, and neighboring $d3$ modules are mirror images of each other, with the axis passing through the center of $d6$ modules. Similarly, the modules are connected in the same way in these five wallpaper groups, so that they can be realized in a single structure (movie S3). Up to this point, the full set of 17 2D space groups can be comprehensively realized using only two modular systems: either the combination of three- and four-unit modules or the combination of four- and six-unit modules.

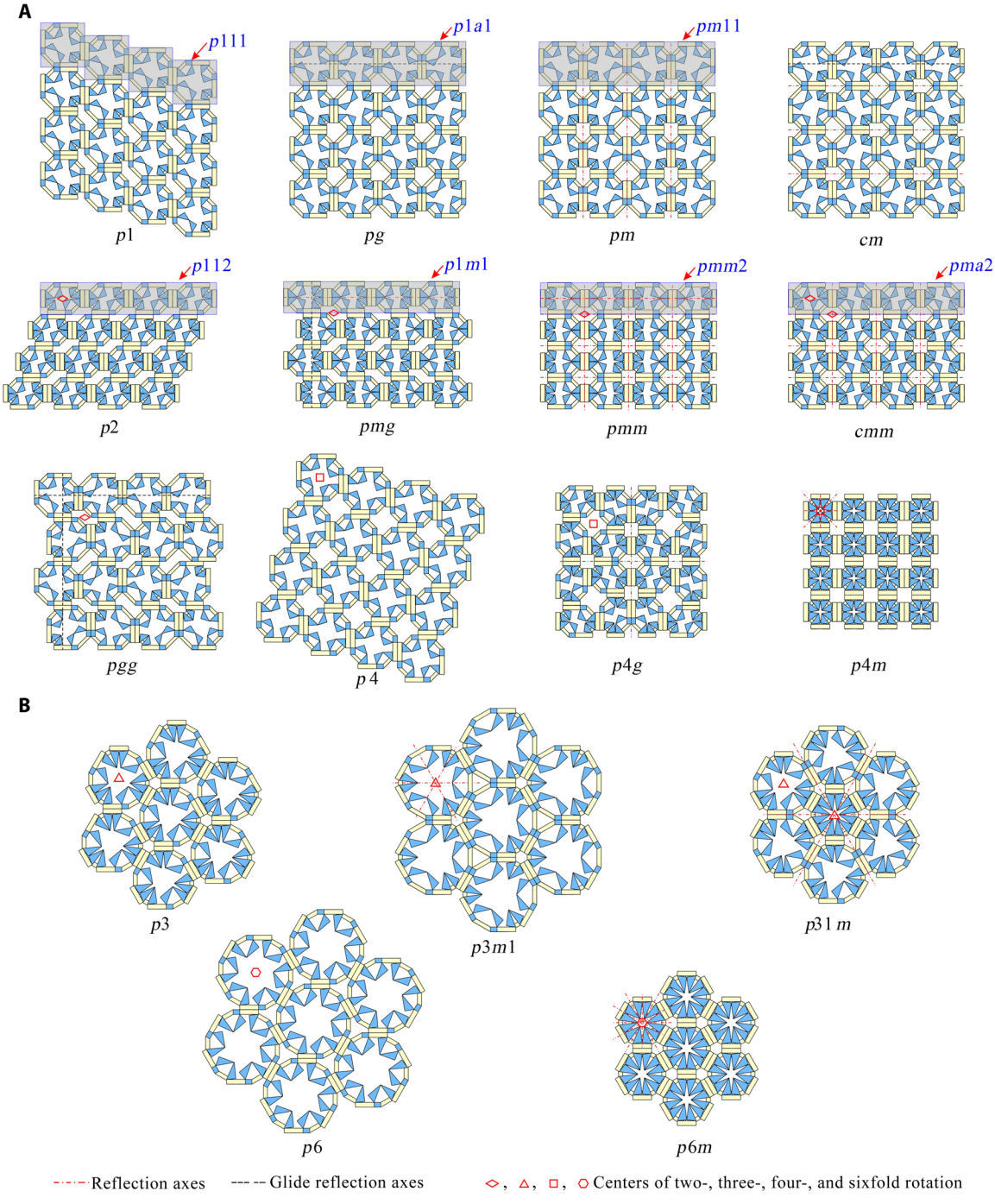

Fig. 3. 2D line and space groups constructed by the four- and six-unit symmetry modules. (**A**) Seven frieze groups (gray area) and 12 wallpaper patterns with distinct symmetry groups constructed by the four-unit symmetry module. (**B**) Five wallpaper patterns with distinct 2D space groups constructed by the six-unit symmetry module. The key reflection axes and glide reflection axes are represented by red center lines and black dotted lines, while the centers of two-, three-, four-, and sixfold rotational symmetry are represented by rhombuses, triangles, squares, and hexagons, respectively.

Actuation methods of the module and tessellation

The inherent kinematic bifurcation enables the proposed origami modules and their tessellations to have diverse configurations with distinct symmetry groups. Our one-DOF origami modules and their tessellations offer a programmable and reversible symmetry tuning strategy with minimal external intervention.

To enable dynamic transitions between symmetry configurations of the four-unit module, we implement a dual-layer pneumatic actuation system comprising 12 independently controllable air pouches, as illustrated in Fig. 4. The upper-layer symmetry selectors consist of eight air pouches (A to H), symmetrically arranged on both sides of the four hinges of the four-unit symmetry module (fabrication

details in Materials and Methods). Without pressurization ($P = 0$, denoted as "0" in the binary coding system), the soft air pouch has negligible thickness and can rotate freely with the origami hinge. Upon pressurization ($P > 0$, denoted as "1"), the air pouch tends to straighten, stiffen, and exert a moment on the hinges, causing the origami module to change shape. It was found that there are a total of three relative orientations for two neighboring triangular panels in a 7*R* unit for all possible configurations for a four-unit symmetry module, i.e., $\varphi_6 = 0$, $\varphi_6 = 90°$, and $\varphi_6 = 180°$, as shown in Fig. 4B. Hence, inflating air pouch B alone (represented by "01") leads to the $\varphi_6 = 90°$ configuration, while inflating air pouch A (represented by "10") alone results in the $\varphi_6 = 180°$ configuration. If both A and B are not pressurized (represented by "00"), then the two neighboring triangular panels will remain in a configuration $\varphi_6 = 0°$. The lower-layer deployment actuators comprise four air pouches (I to L), each embedded in the ice-blue sheets that connect adjacent 7*R* units of the four-unit symmetry module (Fig. 4C). Meanwhile, a prestretched latex loop was added to the thin sheets to form a pneumatic-tendon coupling system enabling reversible folding-unfolding motion, while experimental investigation of interaction between the origami hinge, the latex loop, and the pneumatic air pouch is shown in fig. S14 and text S6. Without pressurization (0), the elastic latex loop keeps the thin sheets tightly attached, maintaining a dihedral angle of 0° (folded state). Upon pressurization (1), the air pouch inflates and separates the thin sheets, increasing the dihedral angle toward 180° (unfolded state). Upon deflation (0), the elastic restoring force retracts the sheets and restores the original folded geometry, enabling fast and reversible shape change. We observe three distinct global shapes of the four connected trapezoidal panels, i.e., a compact square, a rectangle, and an expanded square, as shown in the top view (Fig. 4D). These correspond to binary inputs of "0000," "0101," and "1111," respectively. Together, the upper-layer symmetry selectors and the lower-layer deployment actuators enable programmable symmetry control of the four-unit module within seconds (see Fig. 4E and movie S4). For instance, a fully folded configuration in case I can be attained by retracting the module from the bifurcation configuration in ~1 s by deflating all air pouches, with the control strategy coded as "00000000, 0000." Moreover, partially folded configurations, corresponding to *c*2 and *d*1 point groups, respectively, can be reached from the bifurcation point using the control codes "00010001, 0101" and "00000101, 0101." Similarly, fully unfolded configurations in cases IV, V, VI, and VII, corresponding to *c*4, *d*2, *d*1, and *c*1 point groups, can be achieved with control codes "01010101, 1111," "10001000, 1111," "01000110, 1111," and "01010010, 1111," respectively. Thanks to the kinematic constraints of the module, the system exhibits strong robustness and fault tolerance, and although the synchronization of the air paths is less than perfect, the experimental results show that it all arrives at the target configuration (movie S4).

While our actuation strategy is originally designed to follow strictly defined kinematic paths derived from ideal linkage analysis, we find that the physical system exhibits inherent compliance due to hinge clearances and material flexibility. This structural compliance effectively broadens the feasible transition pathways beyond those directly connected by the ideal bifurcation topology, allowing the system to reversely reconfigure from the compact *d*4 configuration directly to any of the other symmetric configurations, even those not directly connected (see movie S5). Furthermore, the dual-layer pneumatic actuation system also supports continuous geometric transformations that expand or contract the overall configuration (e.g., from a compact square to a rectangle and then to an expanded square or vice versa, as shown in movie S6).

Having demonstrated that the shape of the origami module can be controlled by pressurizing embedded air pouches, we now extend this approach to the 2 × 2 tessellation. As depicted in Fig. 4F and movie S7, we strategically activate air pouches in the upper-layer symmetry selectors and the lower-layer deployment actuators, thereby achieving all 12 configurations corresponding to the 12 wallpaper groups in Fig. 3A through the pressurization of the air pouches based on individual module control rules.

The implementation of this simple binary pressurization strategy using air pouches demonstrates the inherent elegance and robustness of our one-DOF reconfigurable modular origami design. Despite the nonlinear and highly coupled kinematics of the system, the bifurcation behavior of the module can be steered effectively without relying on complex feedback control or synchronization.

Selection rules of multipole qBICs via origami module symmetry tuning

Building on our symmetry-tunable origami platform, we propose a plasmonic origami metasurface composed of copper tetramers with symmetric geometric parameters, periodically arranged on a mechanically reconfigurable substrate made of a flame-retardant organic material (FR4), as illustrated in Fig. 5A. The initial structure (*p*4*m*-90°) exhibits full symmetry, and by tuning the dihedral angle φ_1 (Fig. 5B), we gradually reduce the symmetry to a lower-order group (*pm*-75°, 45°, 15°, and 0°), eliminating rotational symmetry while retaining mirror reflections. To reveal how symmetry governs EM behavior, we investigate the BICs supported by our origami metasurface in the 0.8- to 1.6-GHz range (see text S7 and Materials and Methods for simulation details). BICs are unique resonant modes that exist at frequencies where radiation is allowed, yet they do not radiate because of symmetry-based selection rules (*24*). In our system, when the metasurface retains full symmetric *p*4*m*-90° configuration, the symmetry of the resonant modes is incompatible with that of the free-space radiation channels. This symmetry mismatch prohibits radiation, causing the mode to be perfectly confined inside the structure, i.e., a phenomenon known as a symmetry-protected BIC, characterized by a theoretically infinite quality (*Q*) factor. When the symmetry is gradually broken from *p*4*m*-90° to *pm*-0° by tuning the dihedral angle φ_1, these protective selection rules are lifted. The previously confined mode starts to couple weakly to radiation, becoming a qBIC. This evolution is quantitatively captured in our simulations: The two BICs at ~1.15 and ~1.50 GHz with *Q* factors of 1628 and 1032 at the Γ point evolve into qBIC I and qBIC II, respectively (Fig. 5C). The band structures (Fig. 5D) further confirm the symmetry-governed nature of these resonances, highlighting how the originally degenerate BIC branches split and deform into radiative qBIC bands as the structural symmetry is lowered. The electric field distributions (Fig. 5E) provide additional insight into this transition. In the fully symmetric *p*4*m*-90° configuration, BIC I and BIC II appear as eigenmodes with electric field vectors of equal magnitude and opposite directions (indicated by black arrows), resulting in destructive interference and no net far-field radiation. These modes are strongly confined and exhibit extremely high *Q* factors, leading to ultranarrow linewidths in the transmission spectrum. Therefore, aside from a low-*Q*, broad-linewidth resonance near ~1.2 GHz, originating from the coupling between another

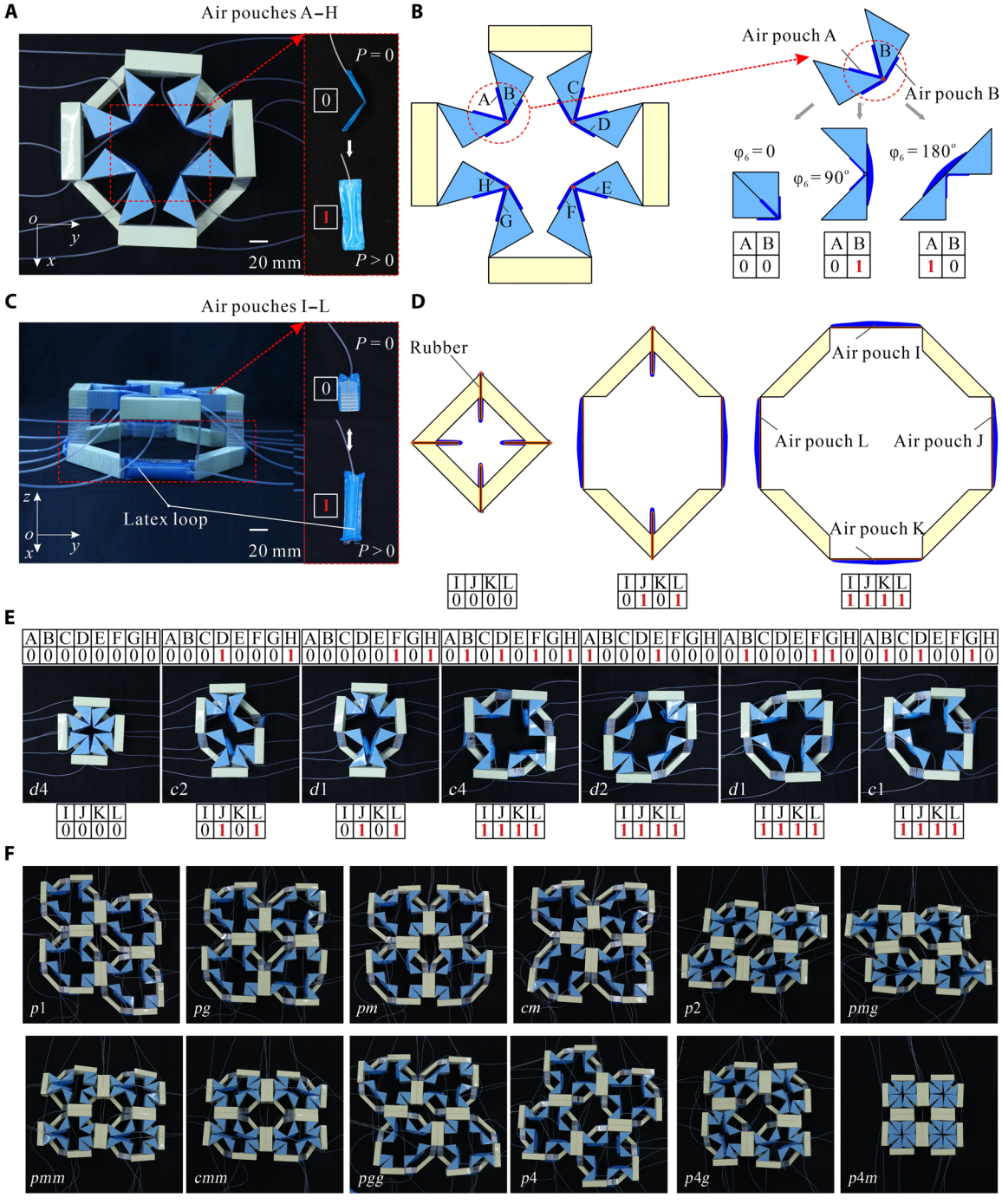

Fig. 4. The symmetry tuned by pneumatic actuation. (**A**) The four-unit symmetry module equipped with eight upper-layer air pouches (A to H), which are symmetrically arranged on both sides of the four hinges. (**B**) Working principle of a pair of upper-layer air pouches: Pressurization induces a moment on the hinges and changes the relative orientation between neighboring triangular panels ($\varphi_6 = 0°$, 90°, or 180°). (**C**) Four lower-layer air pouches (I to L), together with prestretched latex loops, are integrated into the thin sheets connecting adjacent 7*R* units, forming a pneumatic-tendon coupling system that enables reversible folding-unfolding motion. (**D**) Three distinct global configurations, i.e., compact square, rectangle, and expanded square, result from different activation patterns of the lower-layer actuators (binary codes 0000, 0101, and 1111, respectively). (**E**) Experimental results of the four-unit symmetry module with *d*4, *c*2, *d*1, *d*2, *c*4, *d*1, and *c*1 symmetries, where air pouches A to L are coded in binary as 00000000, 0000; 00010001, 0101; 00000101, 0101; 10001000, 1111; 01000110, 1111; 01010101, 1111; and 01010010, 1111, respectively. (**F**) Twelve configurations of distinct symmetry groups of a single 2 × 2 tessellation.

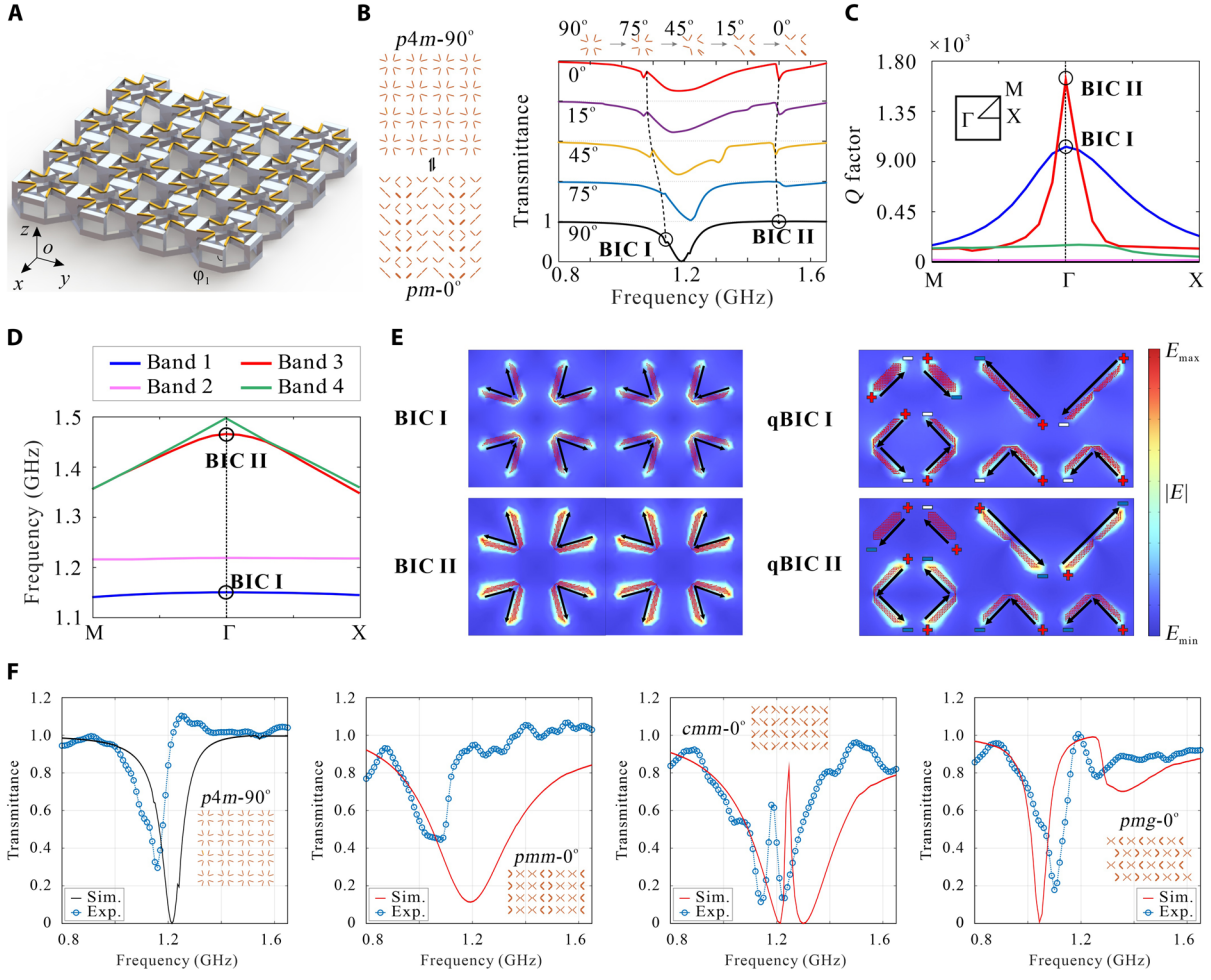

Fig. 5. Motion-sensitive multipole of plasmonic qBICs. (**A**) Schematic of the proposed reconfigurable origami-based metasurface with embedded EM antennas. (**B**) Analytically calculated transmittance of the metasurface as transforming from *p4m*-90° to *pm* (0°, 15°, 45°, and 75°) symmetry group. (**C**) Simulated *Q* factors of the eigenmode in the *k*-space in the vicinity of the Γ point. The inset is the first Brillouin zone. (**D**) Simulated band structure with the eigen frequency of the *p4m*-90° metasurface near the Γ point. (**E**) The spatially resolved electric field intensity distributions and vector orientations of *p4m*-90° and *pm*-0° configurations. Arrows on the EM antenna for qBIC1 and qBIC2 represent electric field intensity distributions. (**F**) Simulated and experimental verification of symmetry-governed selection rules for multipole qBICs. Simulated (solid curves) and experimentally measured (blue dotted lines) transmission spectra of four metasurfaces (configurations *p4m*-90°, *pmm*-0°, *cmm*-0°, and *pmg*-0°) demonstrate the role of symmetry in governing the emergence and tunability of multipole qBICs over the 0.8- to 1.6-GHz frequency range. Sim., simulated; Exp., experimental.

eigenmode and the incident EM wave and unrelated to the BICs, no observable resonance valleys are present in the transmission spectrum for these modes, despite their existence (Fig. 5B). When the symmetry is reduced to *pm*-0°, the original BIC mode undergoes symmetry breaking, resulting in the disruption of the destructive interference condition of the counter-propagating electric field and the generation of a net electric field component. This causes the originally bound energy to radiate outward in the form of a leakage wave, leading to a notable decrease in the *Q* factor and an increase in the resonance linewidth, resulting in typical asymmetric Fabry-Perot resonance valleys qBIC I and qBIC II in the transmission spectrum.

We extended this analysis to 12 different symmetry groups (each with configurations ranging from 90° to 0°), finding that symmetry fundamentally governs the emergence and tunability of qBICs, as shown in fig. S15, while the degree of deformation mainly induces a frequency shift (fig. S16). Figure 5F summarizes the selection rules of BICs via origami module symmetry tuning. First, all trapped BICs, decoupled from the far field, exhibit relatively high symmetry and sufficient compound symmetry (e.g., *p*4*m* and *pmm* have perpendicular reflections but neither local nor global chirality). Taking the simulated EM spectra of *p4m*-90° and *pmm*-0° in Fig. 5F as an example, they display a single, well-defined resonance peak, indicating weak EM coupling within the structure. Second, highly trapped BIC structures benefit from strong global chirality (*p*1, *p*2, and *p*4) or a combination of mirror symmetry and local chirality (*cm*, *cmm*, and *p*4*g*), which produces notable narrow-band resonance characteristics at multiple frequency points. Taking the simulated EM spectra of *cmm*-0° in Fig. 5F as an example, there are multiple deep and narrow resonance peaks, effectively enhancing the localization of EM waves and increasing resonance strength over a broader frequency range. Last, because of the introduction of glide reflection (*pg*, *pmg*, *pgg*, and *p*4*g*), the symmetry of the system is markedly

broken, and the BIC resonance is not fully maximized (partially trapped BIC). For instance, the simulated EM spectra of *pmg*-0° in Fig. 5F display broad and shallow resonance peaks, indicating relatively weak coupling and limited constraint of EM waves. To experimentally validate these findings, we fabricated and characterized four metasurface prototypes corresponding to the simulated configurations (*p4m*-90°, *pmm*-0°, *cmm*-0°, and *pmg*-0°), with a detailed experimental setup presented in text S8 and fig. S17. The measured transmission spectra (blue dotted lines in Fig. 5F) exhibit good agreement with the simulated results (solid curves) in terms of resonance positions and trends, thereby supporting the symmetry-governed selection rules for multipole qBICs. Minor discrepancies in amplitude and linewidth are attributed to the finite size of the fabricated array, which deviates from the ideal infinite periodicity assumed in simulations. This finite-size effect introduces edge scattering and boundary mismatch, slightly shifting resonance frequencies and reducing spectral contrast. In summary, symmetry tuning plays a critical role in modulating system response, enabling highly selective and sensitive BICs and offering insights for designing multifunctional optical devices, particularly for plasmonic-based filters and sensors.

DISCUSSION

In this study, we presented an approach to achieve active tunable symmetry groups in reconfigurable structures via inherent kinematic bifurcation behavior of a single-DOF origami module metasurface and demonstrated its potential application in high-EM selection with multipole qBICs via antenna-integrated plasmonic metasurfaces. A comprehensive kinematic analysis was first conducted on the single-loop modular origami unit to reveal the effect of design parameters on bifurcation behavior. Then, these units can be assembled into various single-DOF modules with folded n-polygon and unfolded $2n$-polygon shapes with bifurcations. Our investigation revealed that it has the potential to realize a variety of discrete symmetry groups, including two families of rosette groups (2D point groups), 7 frieze groups (2D line groups), and 17 wallpaper groups (2D space groups), within a unified design framework. Notably, because of the rich geometry and configurations, two modules, i.e., four- and six-unit symmetry modules, are sufficient to realize 10 crystallographic point groups. The linear tessellation of four-unit symmetry modules is sufficient to realize seven line groups by manipulating the reconfiguration of modules within tessellations. Meanwhile, the planar tessellation of four-unit symmetry modules can realize the first 12 of the 17 space groups with one-, two-, and fourfold rotational symmetry, while the planar tessellation of three- or six-unit symmetry modules can realize the last 5 of the 17 space groups with three- and sixfold rotational symmetry. We also explored whether it is possible to achieve all 17 wallpaper symmetry groups using a single module with a higher number of units because increasing the number of units within a module enhances its point group coverage. However, in practice, the construction of wallpaper groups with different symmetry operations imposes incompatible lattice and connectivity constraints, which results in at least two distinct module architectures to achieve all 17 wallpaper symmetry groups (construction of wallpaper groups with the 12-unit symmetry module is shown in fig. S18). We demonstrated experimentally that the shape and symmetry of such origami modules can be actively tuned and controlled in a completely predictable manner by strategically activating inflatable pouches. To exemplify the potential implications of symmetry group tunability, we further established qBIC selection rules for antenna-integrated plasmonic metasurfaces through EM simulation and experiment, demonstrating how symmetry-engineered reconfigurability directly governs EM multipolar interactions. Because of the current fabrication and system integration limitations, the measurements were performed on discrete, fixed-configuration prototypes rather than on a fully reconfigurable origami platform. However, this approach provides a controlled and rigorous means to isolate and verify the key physical mechanism, i.e., the modulation of multipole qBICs through symmetry tuning, without the confounding factors of actuation and mechanical vibrations. Unlike typical reconfigurable antennas that focus on active modulation of near-field and far-field radiation characteristics, such as frequency tuning, polarization control, and beam steering, achieved via material deformation or structural chaining (*47*–*51*), our work introduces a nonradiative antenna platform integrated with reconfigurable modular origami, enabling high-Q resonances via simple symmetry tuning.

This work introduces a promising paradigm for reconfigurable structures featuring tunable symmetry, which not only broadens the range of tunable symmetry groups within a single structure but also paves the pathway for multifaceted design in multiphysics fields such as electromagnetism. The unique advantage of the single-DOF design lies in its unparalleled simplicity and efficiency, minimizing complex control mechanisms and eliminating the need for structural refabrication. Furthermore, leveraging the modular nature of our origami architecture, where flat sheets are folded into discrete volumetric units, we were able to embed electronic components such as micro air pumps, lithium-ion batteries, and Bluetooth-controlled voltage switches within the origami structure. Control signals can be wirelessly transmitted via Bluetooth, triggering selective pressurization of the embedded pouches and enabling untethered reconfiguration (for fabrication details, see fig. S19). Anticipating future advancements, the integration of 4D printing techniques at the microscale and untethered actuation strategies, such as magnetic, thermal, or optical fields combined with programmable responses, holds the promise of augmenting the versatility and adaptability of the proposed reconfigurable EM antenna-integrated metasurfaces, thereby unveiling intriguing prospects for future exploration and development. Meanwhile, the 17 symmetry groups within a unified design framework proposed here can be used as a cornerstone to deeply explore the intrinsic correlation between symmetry and multiphysical properties of EM, optics, acoustics, etc., which may lead to the establishment of a previously unexplored theoretical framework of interdisciplinary integration.

MATERIALS AND METHODS

Fabrication of the origami module

Patterns of thick-panel components of the four-unit symmetry module were fabricated from thin cardboard first using an efficient laser-cutting technique. Then, they are connected by CPTFEG transparent tape (thickness = 0.08 mm) to form the rectangular blocks (20 mm by 20 mm by 80 mm), triangular panels (the length of the leg = 40 mm, and thickness = 20 mm), and trapezoidal panels (the length of the leg is equal to the lengths of the lateral edge, i.e., 20 mm). Meanwhile, blue thin rectangular sheets (20 mm by 40 mm) were fabricated from polyethylene terephthalate (PET) with a thickness = 1 mm

using a laser-cutting technique. At last, blocks and PET sheets are stuck together with adhesive tape (3M, 8959) to be the four-unit symmetry module.

Fabrication of the pneumatic actuators

To actuate the origami modules, we fabricated air pouches. Initially, the air pouches A to H were formed by placing the edges of two pieces of thermoplastic polyurethane (TPU)–coated fabric (60 mm by 20 mm) (TPU-N20D, Jiaxing Inch Eco Materials Inc., China) of thickness $t = 0.03$ mm into a heat-sealing machine (Deli 16499, Deli Group Co. Ltd., China). To allow inflation, an air tube with a diameter of 1 mm was then inserted and glued into the TPU-coated fabric, before embedding it on two sides of neighboring rectangular panels through double-sided adhesive (3M, 55236). Last, the origami modules were actuated by inflating the air pouches using syringes attached to the air tubes. For the four additional air pouches (I to L), each was integrated into a pneumatic-tendon coupling system consisting of two PET sheets (40 mm by 20 mm and thickness $t = 1$ mm), a central air pouch (identical to pouches A to H), and a prestretched latex loop (diameter = 20 mm; Deli 3212, Deli Group Co. Ltd., China). The latex loop was anchored at both ends of the PET sheets and threaded through the middle section between them under tension.

EM simulation method

This article uses the radio frequency EM frequency domain module of COMSOL Multiphysics for finite element simulation. The metal conductor tetramer material is set to copper, with a conductivity of 5.8×10^7 S/m and a thickness of 0.035 mm. The substrate material is FR4, with a relative dielectric constant of 4.3 and a thickness of 0.6 mm. It is arranged in a periodic manner in the x and y directions. The boundary condition is set to Floquet period, and the z direction is set to air and a perfect matching layer, with thicknesses of 300 and 150 mm, respectively. The x-polarized light is vertically incident on the surface of the element along the z axis, and the grid is set as a physical field control grid. The complex characteristic frequency is calculated from $w = w_0 - i\gamma$, and the Q factor is calculated from $Q = w_0/2\gamma$. The transmission spectrum and field distribution were calculated in the frequency domain through computational research. Frequency domain solution was used to calculate the transmission spectrum and field distribution.

Supplementary Materials

The PDF file includes:
Supplementary Text
Figs. S1 to S19
Tables S1 and S2
Legends for movies S1 to S7

Other Supplementary Material for this manuscript includes the following:
Movies S1 to S7

REFERENCES AND NOTES

1. D. Avnir, D. Huylebrouck, On left and right: Chirality in architecture. *Nexus Netw. J.* **15**, 171–182 (2013).
2. S. P. Seherr-Thoss, H. C. Seherr-Thoss, *Design and Color in Islamic Architecture: Afghanistan, Iran, Turkey* (Smithsonian Institution Press, 1968).
3. C. E. Home, M. A. Hann, The geometrical basis of patterns and tilings: A review of conceptual developments. *J. Text. Inst.* **89**, 27–46 (1998).
4. D. Schattschneider, In black and white: How to create perfectly colored symmetric patterns. *Comput. Math. Appl.* **12**, 673–695 (1986).
5. C. M. Reinke, T. M. De La Mata Luque, M. F. Su, M. B. Sinclair, I. El-Kady, Group-theory approach to tailored electromagnetic properties of metamaterials: An inverse-problem solution. *Phys. Rev. E* **83**, 066603 (2011).
6. Z. Y. Chen, Z. Zhang, S. A. Yang, Y. X. Zhao, Classification of time-reversal-invariant crystals with gauge structures. *Nat. Commun.* **14**, 743 (2023).
7. C. Liang, Y. Rouzhahong, C. Ye, C. Li, B. Wang, H. Li, Material symmetry recognition and property prediction accomplished by crystal capsule representation. *Nat. Commun.* **14**, 5198 (2023).
8. T. Frenzel, M. Kadic, M. Wegener, Three-dimensional mechanical metamaterials with a twist. *Science* **358**, 1072–1074 (2017).
9. L. Lu, S. Leanza, R. R. Zhao, Origami with rotational symmetry: A review on their mechanics and design. *Appl. Mech. Rev.* **75**, 050801 (2023).
10. Y. Mao, Q. He, X. Zhao, Designing complex architectured materials with generative adversarial networks. *Sci. Adv.* **6**, eaaz4169 (2020).
11. A. Montazeri, A. Saeedi, E. Bahmanpour, M. Mahnama, Auxetic mechanical metamaterials with symmetry-broken *re*-entrant units. *Int. J. Mech. Sci.* **266**, 108917 (2024).
12. O. Isik, K. P. Esselle, Analysis of spiral metamaterials by use of group theory. *Metamaterials* **3**, 33–43 (2009).
13. P. Yu, A. S. Kupriianov, V. Dmitriev, V. R. Tuz, All-dielectric metasurfaces with trapped modes: Group-theoretical description. *J. Appl. Phys.* **125**, 143101 (2019).
14. K. Achouri, V. Tiukuvaara, O. J. F. Martin, Spatial symmetries in nonlocal multipolar metasurfaces. *Adv. Photon.* **5**, 046001 (2023).
15. Q. Ren, F. Feng, X. Yao, Q. Xu, M. Xin, Z. Lan, J. You, X. Xiao, W. E. I. Sha, Multiplexing-oriented plasmon-MoS_2 hybrid metasurfaces driven by nonlinear quasi bound states in the continuum. *Opt. Express* **29**, 5384–5396 (2021).
16. M. Liu, D. A. Powell, I. V. Shadrivov, M. Lapine, Y. S. Kivshar, Spontaneous chiral symmetry breaking in metamaterials. *Nat. Commun.* **5**, 4441 (2014).
17. H.-X. Wang, L. Liang, B. Jiang, J. Hu, X. Lu, J.-H. Jiang, Higher-order topological phases in tunable C_3 symmetric photonic crystals. *Photonics Res.* **9**, 1854 (2021).
18. W. A. Benalcazar, B. A. Bernevig, T. L. Hughes, Quantized electric multipole insulators. *Science* **357**, 61–66 (2017).
19. Z.-D. Zhang, M.-H. Lu, Y.-F. Chen, Observation of free-boundary-induced chiral anomaly bulk states in elastic twisted kagome metamaterials. *Phys. Rev. Lett.* **132**, 086302 (2024).
20. G. Librandi, E. Tubaldi, K. Bertoldi, Programming nonreciprocity and reversibility in multistable mechanical metamaterials. *Nat. Commun.* **12**, 3454 (2021).
21. C. Qiao, F. Agnelli, D. K. Pokkalla, N. D'Ambrosio, D. Pasini, Anisotropic morphing in bistable kirigami through symmetry breaking and geometric frustration. *Adv. Mater.* **36**, e2313198 (2024).
22. K. Koshelev, S. Lepeshov, M. Liu, A. Bogdanov, Y. Kivshar, Asymmetric metasurfaces with high-*Q* resonances governed by bound states in the continuum. *Phys. Rev. Lett.* **121**, 193903 (2018).
23. A. C. Overvig, S. C. Malek, M. J. Carter, S. Shrestha, N. Yu, Selection rules for quasibound states in the continuum. *Phys. Rev. B* **102**, 35434 (2020).
24. J. Wang, P. Li, X. Zhao, Z. Qian, X. Wang, F. Wang, X. Zhou, D. Han, C. Peng, L. Shi, J. Zi, Optical bound states in the continuum in periodic structures: Mechanisms, effects, and applications. *Photonics Insights* **3**, R01 (2024).
25. D. Han, W. Li, M. Liu, T. Sun, Y. Hou, X. Chen, H. Shi, Z. Fan, X. Wang, F. Meng, L. Zhang, X. Chen, Kirigami-inspired planar deformable metamaterials for multiple dynamic electromagnetic manipulations. *Laser Photonics Rev.* **17**, 2300374 (2023).
26. Y. Chen, W. Ye, R. Xu, Y. Sun, J. Feng, P. Sareh, A programmable auxetic metamaterial with tunable crystal symmetry. *Int. J. Mech. Sci.* **249**, 108249 (2023).
27. R. He, Y. Chen, J. Liang, Y. Sun, J. Feng, P. Sareh, Crystallographically programmed kirigami metamaterials. *J. Mech. Phys. Solids* **193**, 105903 (2024).
28. M. Schenk, S. D. Guest, Geometry of miura-folded metamaterials. *Proc. Natl. Acad. Sci. U.S.A.* **110**, 3276–3281 (2013).
29. M. Eidini, G. H. Paulino, Unraveling metamaterial properties in zigzag-base folded sheets. *Sci. Adv.* **1**, e1500224 (2015).
30. J. T. B. Overvelde, T. A. De Jong, Y. Shevchenko, S. A. Becerra, G. M. Whitesides, J. C. Weaver, C. Hoberman, K. Bertoldi, A three-dimensional actuated origami-inspired transformable metamaterial with multiple degrees of freedom. *Nat. Commun.* **7**, 10929 (2016).
31. R. Peng, G. S. Chirikjian, Thick-panel origami structures forming seamless surfaces. *Nat. Commun.* **16**, 3881 (2025).
32. Z. Wang, L. Jing, K. Yao, Y. Yang, B. Zheng, C. M. Soukoulis, H. Chen, Y. Liu, Origami-based reconfigurable metamaterials for tunable chirality. *Adv. Mater.* **29**, 1700412 (2017).
33. H. Feng, W. Lv, J. Ma, W. Chang, Y. Chen, J. Wang, Helical structures with switchable and hierarchical chirality. *Appl. Phys. Lett.* **116**, 194102 (2020).
34. J. T. B. Overvelde, J. C. Weaver, C. Hoberman, K. Bertoldi, Rational design of reconfigurable prismatic architected materials. *Nature* **541**, 347–352 (2017).
35. Y. Miyazawa, H. Yasuda, H. Kim, J. H. Lynch, K. Tsujikawa, T. Kunimine, J. R. Raney, J. Yang, Heterogeneous origami-architected materials with variable stiffness. *Commun. Mater.* **2**, 110 (2021).
36. K. Liu, P. P. Pratapa, D. Misseroni, T. Tachi, G. H. Paulino, Triclinic metamaterials by tristable origami with reprogrammable frustration. *Adv. Mater.* **34**, e2107998 (2022).

37. Y. Li, A. Di Lallo, J. Zhu, Y. Chi, H. Su, J. Yin, Adaptive hierarchical origami-based metastructures. *Nat. Commun.* **15**, 6247 (2024).
38. L. Liu, G. P. T. Choi, L. Mahadevan, Wallpaper group kirigami. *Proc. R. Soc. A Math. Phys. Eng. Sci.* **477**, 20210161 (2021).
39. A. Jamalimehr, M. Mirzajanzadeh, A. Akbarzadeh, D. Pasini, Rigidly flat-foldable class of lockable origami-inspired metamaterials with topological stiff states. *Nat. Commun.* **13**, 1816 (2022).
40. Y. Yang, Z. You, Geometry of transformable metamaterials inspired by modular origami. *J. Mech. Robot.* **10**, 021001 (2018).
41. D. Mousanezhad, S. Kamrava, A. Vaziri, Origami-based building blocks for modular construction of foldable structures. *Sci. Rep.* **7**, 14792 (2017).
42. Y. Li, Q. Zhang, Y. Hong, J. Yin, 3D transformable modular kirigami based programmable metamaterials. *Adv. Funct. Mater.* **31**, 2105641 (2021).
43. J. Ma, X. Jiang, Y. Chen, A 3D modular meta-structure with continuous mechanism motion and bistability. *Extreme Mech. Lett.* **51**, 101584 (2022).
44. K. Xiao, Z. Liang, B. Zou, X. Zhou, J. Ju, Inverse design of 3D reconfigurable curvilinear modular origami structures using geometric and topological reconstructions. *Nat. Commun.* **13**, 7474 (2022).
45. Y. Zhu, E. T. Filipov, Large-scale modular and uniformly thick origami-inspired adaptable and load-carrying structures. *Nat. Commun.* **15**, 2353 (2024).
46. P. Kumar, S. Pellegrino, Computation of kinematic paths and bifurcation points. *Int. J. Solids Struct.* **37**, 7003–7027 (2000).
47. D. Rodrigo, B. A. Cetiner, L. Jofre, Frequency, radiation pattern and polarization reconfigurable antenna using a parasitic pixel layer. *IEEE Trans. Antennas Propag.* **62**, 3422–3427 (2014).
48. H. Fu, K. Nan, W. Bai, W. Huang, K. Bai, L. Lu, C. Zhou, Y. Liu, F. Liu, J. Wang, M. Han, Z. Yan, H. Luan, Y. Zhang, Y. Zhang, J. Zhao, X. Cheng, M. Li, J. W. Lee, Y. Liu, D. Fang, X. Li, Y. Huang, Y. Zhang, J. A. Rogers, Morphable 3D mesostructures and microelectronic devices by multistable buckling mechanics. *Nat. Mater.* **17**, 268–276 (2018).
49. S. Lee, S. I. H. Shah, H. L. Lee, S. Lim, Frequency-reconfigurable antenna inspired by origami flasher. *IEEE Antennas Wireless Propag. Lett.* **18**, 1691–1695 (2019).
50. A. M. Sadiq, Y. Gu, Y. Luo, Y. Chen, K. Ma, Gain-enhanced reconfigurable radiation array with mechanically driven system and directive elements. *Front Mech Eng* **17**, 60 (2022).
51. X. Zhang, J. Ma, M. Li, Z. You, X. Wang, Y. Luo, K. Ma, Y. Chen, Kirigami-based metastructures with programmable multistability. *Proc. Natl. Acad. Sci. U.S.A.* **119**, e2117649119 (2022).

Acknowledgments: We thank J. Yang from Seoul National University for helpful discussions. **Funding:** Y.C. acknowledges the support of the National Natural Science Foundation of China (grant nos. 52320105005 and 52035008) and the New Cornerstone Science Foundation through the XPLORER PRIZE (grant XPLORER-2020-1035). W.L. acknowledges the support of the National Key R&D Program of China (grant no. 2024YFB4707300). H.J. acknowledges the National Natural Science Foundation of China (grant no. 12350003). **Author contributions:** Conceptualization: W.L. and Y.C. Methodology: W.L., Q.R., H.H., and Y.C. Validation: W.L., Y.W., H.H., Q.R., and Y.L. Visualization: W.L., H.H., Y.C., and Q.R. Writing—original draft: W.L., Y.C., and Q.R. Writing—review and editing: W.L., Y.C., and J.M. Supervision: Y.C., Q.R., J.M., Z.Z., H.J., and X.W. Project administration: Y.C. Funding acquisition: Y.C. and H.J. **Competing interests:** The authors declare that they have no competing interests. **Data and materials availability:** All data needed to evaluate the conclusions in the paper are present in the paper and/or the Supplementary Materials.

Submitted 19 April 2025
Accepted 14 October 2025
Published 12 November 2025
10.1126/sciadv.ady3812